ELSEVIER

Optimal design of box-section sandwich beams in three-point bending

S.P. Mai, N.A. Fleck *, T.J. Lu [1]

Department of Engineering, University of Cambridge, Trumpington Street, Cambridge CB2 1PZ, UK

Abstract

Minimum mass designs are obtained for box-section sandwich beams of various cross-sections in three-point bending. The overall compliance of the hollow, tubular beams are decomposed additively into a global contribution due to macroscopic bending (Timoshenko beam theory) and a local contribution associated with transverse deflection of the walls of the hollow beam adjacent to the central loading patch. The structural response is analysed for beams of square sections with various internal topologies: a solid section, a foam-filled tube with monolithic walls, a hollow tube with walls made from sandwich plates, and a hollow tube with walls reinforced by internal stiffeners. Finite element analysis is used to validate analytical models for the overall stiffness of the tubes in three-point bending. Minimum mass designs are obtained as a function of the overall stiffness, and the relative merits of the competing topologies are discussed.
© 2006 Elsevier Ltd. All rights reserved.

Keywords: Sandwich structures; Optimal design; Finite element method; Lattice materials; Elasticity theory; Local compliance

1. Introduction

Hollow tubes possess an efficient shape for engineering components due to their high inherent bending and torsional rigidities. For example, box-section steel girders are a familiar design of beams in bridges and other civil engineering structures. Currently, industrial interest exists in the use of tubes with sandwich walls for the moving head of a milling machine (HyMM project),[2] see Meo et al. (2005) and Srikantha Phani et al. (2006). To date, milling machine heads have the topology of rectangular tubes with monolithic walls. The head contains the cutting motor and moves on guide-rails. The overall compliance of the milling head is partly due to macroscopic bending of the tube and partly due to the local compliance at the supports on the guide-rails.

Internal stiffeners support the monolithic walls of the tube and increase the local bending stiffness adjacent to the supports. An alternative strategy, as yet untried, is to use sandwich construction for the walls. Although the structural benefit of sandwich plates and shells with lattice cores have been highlighted (Deshpande and Fleck, 2001; Evans et al., 2001; Wadley et al., 2003; Wicks and Hutchinson, 2001; Zok et al., 2003), little is known about the performance of tubes with sandwich walls. The potential of sandwich construction for tubes in three-point bending is explored herein, with the milling machine application in mind.

Lightweight sandwich beams and panels can be designed through use of stochastic cores (metallic and polymeric foams) or periodic lattice-cores (pyramidal, tetrahedral and textile). Minimum mass designs can be obtained for any given loading configuration such as three-point bending. The optimal geometry depends upon whether the design is *stiffness-limited* (Ashby et al., 2000; Gibson and Ashby, 1997; Zenkert, 1995) or *strength-limited* (Ashby et al., 2000; Deshpande and Fleck, 2001; Gibson and Ashby, 1997; Wadley et al., 2003; Wicks and Hutchinson, 2001; Zenkert, 1995; Zok et al., 2003). In stiffness-governed design, the geometric and material parameters of the sandwich panel are optimised in order to achieve a minimum mass for a given value of non-dimensional stiffness, termed the *stiffness index*.

In strength-governed design, competing failure mechanisms such as face yield, face wrinkling, core shear, and face indentation are each a function of the geometrical and material properties. It is often useful to construct a collapse mechanism map with geometric parameters as axes; the map displays the active failure mechanisms, with contours of structural load index and mass superimposed. A trajectory of minimum mass can be identified on the map, with the structural load index varying along this trajectory. In general, the active failure mode changes with the magnitude of the structural load index. Consider, for example, the plastic collapse of a sandwich beam with solid metallic faces and a tetrahedral lattice core. Deshpande and Fleck (2001) have derived minimum mass designs for the case of three-point bending. As the load carrying capacity is increased, the dominant failure model switches from combined face yield/face wrinkling to combined face yield/indentation and then to combined core shear/indentation.

Budiansky (1999) has evaluated the strength-limited minimum mass design of several monolithic and sandwich structures under axial compression. Reduced mass is obtained at low values of load index by using sandwich construction as the walls of hollow columns, or as the faces and stringers of stiffened panels. However, the optimised designs tend to be impractical because they require sheets of thin gauge for the core and facesheet. This can be traced to the simplifying assumption that details on load introduction at the supports have been ignored. The sensitivity of stiffness-limited minimum mass design to the support details is explored in the current study.

The scope of this paper is as follows. First, in Section 2, we define the problem of *stiffness-governed design* of a beam in three-point bending. The minimum mass optimisation task is defined for a square beam with selected internal topologies: a solid section, a foam-filled tube with monolithic walls, a hollow sandwich-walled tube, and a hollow tube with rib-reinforced walls. In Section 3, Timoshenko beam theory is used to determine the bending and shear stiffness of each beam, and to obtain the optimal solution for each topology. In Section 4, the overall compliance of the tube in three-point bending is taken to be the sum of the macroscopic compliance by Timoshenko beam theory and the local contribution of the walls near the central loading patch. Optimal solutions are again obtained for all topologies and it is shown that inclusion of the local compliance switches the optimal topology. In Section 5, the sensitivity of the optimised designs to an additional constraint on the internal width of the hollow tube is explored.

It is appreciated that the analysis given in this study is highly idealised and neglects the effects of attachment details and manufacturing imperfections. Additional design variables such as strength, cost and manufacturability are also ignored. Nevertheless, the study highlights the importance of including local compliance in the structural optimisation, and indicates the potential of sandwich construction for tubes in bending, particularly when the details of load introduction are included.

2. Statement of problem

2.1. Geometry of beam in three-point bending

Consider the prototypical problem of a uniform beam of square solid cross-section (width and depth equal to *b*) loaded in three-point bending. This mimics the loading configuration for a milling machine head. Idealise
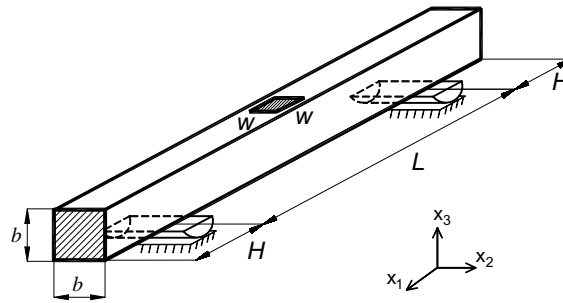
Fig. 1. Square solid beam in three-point bending.

the loading on the beam at mid-span by a lateral uniform pressure q distributed over a square patch ($w \times w$) at the centre of the upper surface to give a load $P = qw^2$, as shown in Fig. 1. The span between the outer supports is L (assume that $w \ll L$) and the overhang distance beyond each of the outer supports is H. Split cylinders of diameter $D = L/20$ form the outer supports; these allow for rotation but are sufficiently large to give negligible local indentation of the beam. In contrast, the concentrated loading at mid-span generates both macroscopic bending of the beam and local displacements associated with transverse deflections of the upper face of the tube. We shall derive analytic expressions for the macroscopic displacement u_m due to the overall bending and shearing of the beam, and the additional contribution u_l due to the *local compliance* of the tube in the vicinity of the central patch load. It is shown in subsequent sections that this local additional compliance is of major significance. The total deflection of the beam at mid-span is $u_t = u_m + u_l$, and the overall *structural stiffness* of the beam is $S \equiv P/u_t$.

2.2. Choice of beam cross-section

A series of optimisation tasks are reported for beams of square cross-sections, in both hollow and solid forms.

Topology A: a beam of solid square cross-section, see Fig. 2a. The beam comprises an isotropic elastic solid with Young's modulus E, Poisson ratio v, and density ρ.

Topology B: a hollow tube with monolithic walls and a foam-filled core, Fig. 2b. The walls are made from the same isotropic elastic solid as that for the beam of topology A of solid cross-section, with material parameters (E, v, ρ). The isotropic foam core has a Young's modulus E_c, Poisson ratio v_c, and density ρ_c.

Topology C: a hollow tube with foam-cored sandwich walls, Fig. 2c. The facesheets and foam are made from isotropic elastic solids with material constants (E, v, ρ) and (E_c, v_c, ρ_c), respectively.

Topology D: a hollow tube with sandwich walls comprising a lattice *square honeycomb* core, Fig. 2d. The sandwich walls are made from an isotropic elastic solid with Young's modulus E, Poisson ratio v, and density ρ. The square honeycomb core of the sandwich is constructed from sheets of the same solid with properties (E, v, ρ).

Topology E: a hollow tube with sandwich panel walls comprising a lattice *corrugated* core, Fig. 2e. Both the facesheets and core are constructed from elastic solid sheets of Young's modulus E, Poisson ratio v, and density ρ.

Topology F: a hollow tube with rib-stiffened monolithic walls, Fig. 2f. Again, the walls are made from an isotropic elastic solid with material constants (E, v, ρ).

2.3. Optimisation task

The mass m of the beam can be written in the non-dimensional form $\overline{m} \equiv m/\rho L^3$, while the non-dimensional stiffness index reads $\overline{S} \equiv S/EL$. The aim of this study is to obtain designs for the beams of topologies A to F in three-point bending such that $\overline{m}$ is minimised for a prescribed value of $\overline{S}$. The optimisation on geometry is constrained by imposing practical limits. For example, the outer width B_{out} of the beam must exceed the fixed
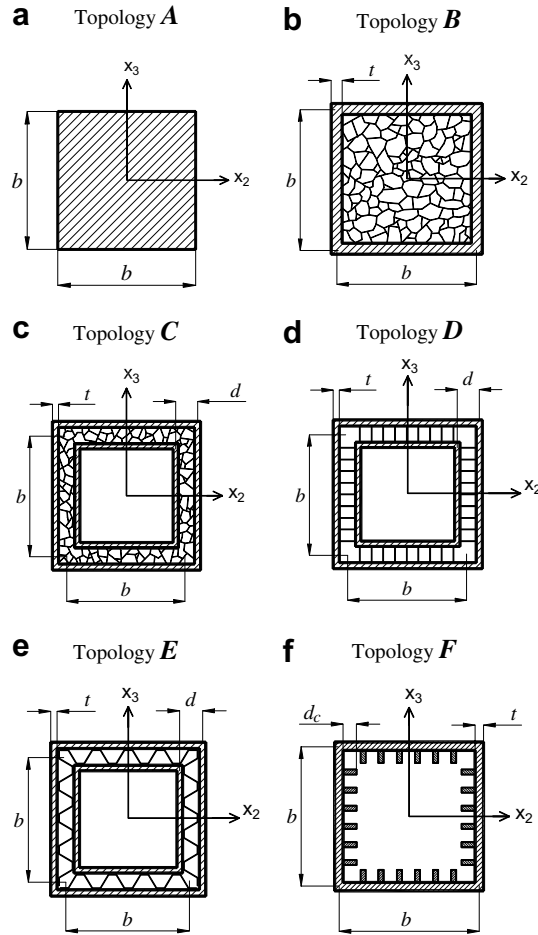
Fig. 2. Square cross-section of a beam with various internal topologies: (a) a solid cross-section; (b) a foam-filled tube; (c) a hollow tube with foam-cored sandwich walls; a hollow tube with sandwich walls comprising a (d) *square honeycomb* or (e) a *corrugated* core; and (f) a hollow tube with rib-stiffened walls.

width $w \equiv 0.05L$ of the loading patch, and it must not be too large to make the beam excessively stubby.[3] Upon introducing the non-dimensional form $\overline{B}_{out} \equiv B_{out}/L$, the stubbiness limit dictates $\overline{B}_{out} \leqslant 0.25$, and we conclude that $\overline{B}_{out}$ is constrained to lay in the range

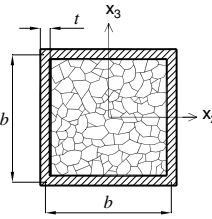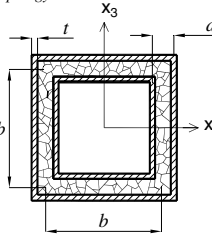$$0.05 \leqslant \overline{B}_{out} \leqslant 0.25. \tag{1}$$
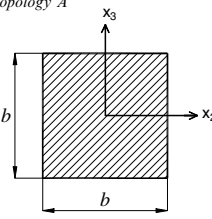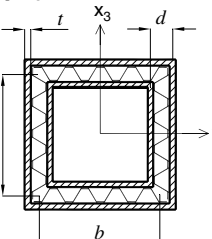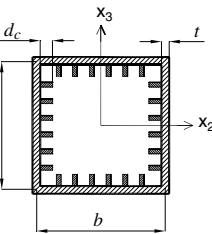
Explicit expressions for $\overline{B}_{out}$ are listed in Table 1 for each topology. For topologies B to F, there exists a lower practical limit on the ratio of the wall thickness t to the tube width b in order to avoid local indentation and panel vibration. By introducing the non-dimensional wall thickness $\overline{t} \equiv t/L$ and non-dimensional tube width $\overline{b} \equiv b/L$, the acceptable range of value for t is stated by

$$e_1 \leqslant \frac{\overline{t}}{\overline{b}} \leqslant 1, \tag{2}$$

where the wall thickness ratio e_1 is taken to be 1/400.

---

[3] The relation between B_{out} and the width dimension b varies from one topology to the next and depends upon other geometrical parameters. For the solid square cross-section, we have $B_{out} = b$, see Fig. 2a.

Table 1
Sectional properties of topologies *A* to *F*

Topology A

$$\overline{B}_{out} = \overline{b} \quad \overline{Gb} = \frac{\overline{b}}{2(1+v)} \quad \overline{GA} = \frac{\overline{b}^2}{2(1+v)}$$

$$\overline{EI} = \frac{\overline{b}^4}{12} \quad \overline{EQ} = \frac{\overline{b}^3}{8} \quad \alpha_s = 1.5$$

Topology B

$$\overline{B}_{out} = \overline{b} + \overline{t} \quad (\overline{Gb})_{eq} = \frac{\overline{t}}{(1+v)} + \frac{E_c}{E}\frac{(\overline{b}-\overline{t})}{2(1+v_c)}$$

$$(\overline{GA})_{eq} = \frac{2\overline{b}\overline{t}}{(1+v)} + \frac{E_c}{E}\frac{(\overline{b}-\overline{t})^2}{2(1+v_c)}$$

$$(\overline{EI})_{eq} = \frac{1}{12}\left\{(\overline{b}+\overline{t})^4 - (\overline{b}-\overline{t})^4\right\} + \frac{E_c}{12E}(\overline{b}-\overline{t})^4$$

$$(\overline{EQ})_{eq} = \frac{1}{8}\left\{(\overline{b}+\overline{t})^3 - (\overline{b}-\overline{t})^3\right\} + \frac{E_c}{8E}(\overline{b}-\overline{t})^3$$

Topology C

$$\overline{B}_{out} = \overline{b} + \overline{d} + \overline{t} \quad (\overline{Gb})_{eq} = \frac{2\overline{t}}{(1+v)} + \frac{E_c}{E}\frac{(\overline{d}-\overline{t})}{(1+v_c)}$$

$$(\overline{GA})_{eq} = \frac{4\overline{b}\overline{t}}{(1+v)} + \frac{2E_c}{E}\frac{\overline{b}(\overline{d}-\overline{t})}{(1+v_c)}$$

$$(\overline{EI})_{eq} = \frac{1}{12}\left\{(\overline{b}+\overline{d}+\overline{t})^4 - (\overline{b}+\overline{d}-\overline{t})^4 + (\overline{b}-\overline{d}+\overline{t})^4 - (\overline{b}-\overline{d}-\overline{t})^4\right\} + \frac{E_c}{12E}\left\{(\overline{b}+\overline{d}-\overline{t})^4 - (\overline{b}-\overline{d}+\overline{t})^4\right\}$$

$$(\overline{EQ})_{eq} = \frac{1}{8}\left\{(\overline{b}+\overline{d}+\overline{t})^3 - (\overline{b}+\overline{d}-\overline{t})^3 + (\overline{b}-\overline{d}+\overline{t})^3 - (\overline{b}-\overline{d}-\overline{t})^3\right\} + \frac{E_c}{8E}\left\{(\overline{b}+\overline{d}-\overline{t})^3 - (\overline{b}-\overline{d}+\overline{t})^3\right\}$$

Topologies D and E

$$\overline{B}_{out} = \overline{b} + \overline{d} + \overline{t} \quad (\overline{Gb})_{eq} = \frac{2\overline{t}}{(1+v)} + \frac{2G_{12}^c}{E}(\overline{d}-\overline{t})$$

$$(\overline{GA})_{eq} = \frac{4\overline{b}\overline{t}}{(1+v)} + \frac{2(G_{12}^c + G_{13}^c)}{E}\overline{b}(\overline{d}-\overline{t})$$

$$(\overline{EI})_{eq} = \frac{1}{12}\left\{(\overline{b}+\overline{d}+\overline{t})^4 - (\overline{b}+\overline{d}-\overline{t})^4 + (\overline{b}-\overline{d}+\overline{t})^4 - (\overline{b}-\overline{d}-\overline{t})^4\right\} + \frac{E_{11}^c}{12E}\left\{(\overline{b}+\overline{d}-\overline{t})^4 - (\overline{b}-\overline{d}+\overline{t})^4\right\}$$

$$(\overline{EQ})_{eq} = \frac{1}{8}\left\{(\overline{b}+\overline{d}+\overline{t})^3 - (\overline{b}+\overline{d}-\overline{t})^3 + (\overline{b}-\overline{d}+\overline{t})^3 - (\overline{b}-\overline{d}-\overline{t})^3\right\} + \frac{E_{11}^c}{8E}\left\{(\overline{b}+\overline{d}-\overline{t})^3 - (\overline{b}-\overline{d}+\overline{t})^3\right\}$$

Topology F

$$\overline{B}_{out} = \overline{b} + \overline{t} \quad (\overline{Gb})_{eq} = \frac{\overline{t}}{(1+v)} + \frac{2G_{12}^c}{E}\overline{d}_c$$

$$(\overline{GA})_{eq} = \frac{2\overline{b}\overline{t}}{(1+v)} + \frac{2(G_{12}^c + G_{13}^c)}{E}(\overline{b}-\overline{t}-\overline{d}_c)\overline{d}_c$$

$$(\overline{EI})_{eq} = \frac{1}{12}\left\{(\overline{b}+\overline{t})^4 - (\overline{b}-\overline{t})^4\right\} + \frac{E_{11}^c}{12E}\left\{(\overline{b}-\overline{t})^4 - (\overline{b}-\overline{t}-2\overline{d}_c)^4\right\}$$

$$(\overline{EQ})_{eq} = \frac{1}{8}\left\{(\overline{b}+\overline{t})^3 - (\overline{b}-\overline{t})^3\right\} + \frac{E_{11}^c}{8E}\left\{(\overline{b}-\overline{t})^3 - (\overline{b}-\overline{t}-2\overline{d}_c)^3\right\}$$

The Poisson ratio for the solid, v, and foam, v_c, are both taken to be 0.3. The density ρ_c of the cores (either metal foam, square honeycomb, corrugated or stiffeners) is an additional variable in the optimisation of topologies B to F. For all topologies, a sequential quadratic programming algorithm is used, as implemented within the optimisation tool-box of Matlab (Mathworks 7, 2004).

3. Optimisation of the six topologies using Timoshenko beam theory

We begin by using Timoshenko beam theory to obtain analytical expressions for the macroscopic bending and shearing stiffness of the beams, with local compliance near the central loading patch neglected. Topologies A to F are considered in turn, and minimum mass designs are obtained for each. Later, the optimisation is repeated with the effects of local compliance included.

Consider a beam in three-point bending. The beam has an *equivalent flexural rigidity* $(EI)_{eq}$ and an *equivalent shearing rigidity* $(GA)_{eq}/\alpha_s$, where α_s is the *shear coefficient* for the beam (Timoshenko and Gere, 1972). The macroscopic mid-span deflection u_m of the beam is the sum of flexural and shear deflections as

$$u_m = \frac{PL^3}{48(EI)_{eq}} + \frac{\alpha_s PL}{4(GA)_{eq}}. \tag{3}$$

The non-dimensional deflection $\bar{u}_m$ reads $\bar{u}_m \equiv u_m EL/P$. Recall that the non-dimensional macroscopic stiffness is $\bar{S} = S/EL$. Consequently, $\bar{S}$ is related to $\bar{u}_m$ by $\bar{S} = 1/\bar{u}_m$. We proceed by evaluating $(EI)_{eq}$ and $(GA)_{eq}/\alpha_s$ for each topology in turn.

3.1. Topology A: a beam with a square, solid cross-section

For a monolithic beam with a square cross-section of width b (Fig. 2a), made of an isotropic elastic with Young's modulus E, we have

$$(EI)_{eq} = EI, \quad (GA)_{eq} = GA, \quad \text{and} \quad \alpha_s = 1.5, \tag{4}$$

where $I = b^4/12$ is the second moment of area, $A = b^2$ is the cross-sectional area. The *shear coefficient* α_s is the numerical factor by which the average shear strain must be multiplied to obtain the maximum shear strain at the neutral axis of the cross-section, and is discussed further in Appendix A. The non-dimensional macroscopic stiffness of the beam is $\bar{S} = S/EL$ and substitution into Eq. (3) gives an expression for $\bar{b} \equiv b/L$ as

$$\bar{b} = \frac{1}{2}\left\{\alpha_s(1+v)\bar{S} + [\alpha_s^2(1+v)^2\bar{S}^2 + 4\bar{S}]^{1/2}\right\}^{1/2}. \tag{5}$$

The stiffness index $\bar{S}$ is chosen over the practical range $\bar{S} = 0$–10^{-3}. No optimisation step is required to obtain the non-dimensional mass $\bar{m} \equiv m/\rho L^3$. At low value of $\bar{S}$ such that $\bar{S} \leqslant 2.48 \times 10^{-5}$, the outer width $\bar{B}_{out} \equiv \bar{b}$ is constrained to equal the patch size, $\bar{B}_{out} \equiv 0.05$, and we obtain

$$\bar{m} = \bar{b}^2 = 0.0025. \tag{6a}$$

For $\bar{S}$ greater than 2.48×10^{-5}, $\bar{B}_{out} \equiv \bar{b}$ is given by Eq. (5) and

$$\bar{m} = \frac{1}{4}\left\{\alpha_s(1+v)\bar{S} + [\alpha_s^2(1+v)^2\bar{S}^2 + 4\bar{S}]^{1/2}\right\}. \tag{6b}$$

3.2. Topology B: a beam made from a square hollow tube and a foam-filled core

Now consider a hollow foam-filled tube of square cross-section as shown in Fig. 2b. The tube is of width b and wall thickness t. The foam core is assumed to be isotropic, homogeneous, and linear elastic. Its Young's modulus E_c scales with the relative density $\bar{\rho}_c = \rho_c/\rho$ according to (Ashby et al. (2000))

$$\frac{E_c}{E} = \bar{\rho}_c^2. \tag{7}$$

In order to determine the mid-span deflection u_m of the beam as given by Eq. (3), a straightforward strength of materials approach is used to calculate $(EI)_{eq}$, $(GA)_{eq}$, and α_s, see for example, Timoshenko and Gere (1972) or Allen (1969). The method is summarised in Appendix A. The *equivalent flexural rigidity* $(EI)_{eq}$ is defined by the sum of the flexural rigidities E_iI_i for each layer i

$$(EI)_{eq} = \sum_i E_iI_i. \tag{8}$$

Similarly, $(GA)_{eq}$ is the sum of the product of shear modulus G_i and cross-sectional area A_i of each layer i

$$(GA)_{eq} = \sum_i G_iA_i. \tag{9}$$

Consider a representative ith layer. Then, Q_i is the first moment about the neutral axis of the portion of the cross-sectional area above the neutral axis, and b_i is the width on the neutral plane. In Appendix A the shear coefficient α_s is defined as

$$\alpha_s \equiv \frac{(EQ)_{eq}}{(EI)_{eq}} \frac{(GA)_{eq}}{(Gb)_{eq}}, \tag{10}$$

where

$$(EQ)_{eq} = \sum_i E_iQ_i \tag{11}$$

and

$$(Gb)_{eq} = \sum_i G_ib_i. \tag{12}$$

Alternatively, by applying the principal of virtual work, the shear deflection is obtained in terms of the *form factor* for shear f_s (Timoshenko and Gere (1972)) rather than the shear coefficient α_s. In general, f_s is slightly different from α_s, and gives a somewhat more accurate value for shear deflection. However, the algebraic formulae involved in writing f_s are unwieldy, and we prefer in this study to use the much simpler approach of defining α_s for sandwich beams. The deflection due to shear is small within the practical range, and so this approach is justified.

The optimisation task is to find the geometrical and material variables that minimise the mass of the foam-filled tube for any given value of stiffness index $\overline{S}$. The geometry is defined by the non-dimensional tube width $\overline{b}$ and wall thickness $\overline{t}$

$$\overline{b} \equiv b/L \quad \text{and} \quad \overline{t} \equiv t/L \tag{13}$$

Now substitute the expression (10) for α_s into Eq. (3). The non-dimensionalised mid-span deflection of the beam reads

$$\overline{u}_m \equiv \frac{1}{\overline{S}} = \frac{1}{48(\overline{EI})_{eq}} + \frac{(\overline{EQ})_{eq}}{4(\overline{EI})_{eq}(\overline{Gb})_{eq}}, \tag{14}$$

where the dimensionless properties of the cross-section are

$$(\overline{EI})_{eq} \equiv \frac{(EI)_{eq}}{EL^4}, \quad (\overline{EQ})_{eq} \equiv \frac{(EQ)_{eq}}{EL^3}, \quad (\overline{GA})_{eq} \equiv \frac{(GA)_{eq}}{EL^2}, \quad \text{and} \quad (\overline{Gb})_{eq} \equiv \frac{(Gb)_{eq}}{EL}. \tag{15}$$

Explicit expressions for these non-dimensional beam properties are listed in Table 1 for topology *B*. (For completeness, similar expressions are given in Table 1 for the remaining topologies *C* to *F*, with details for these topologies are given in the following sections).

The objective function is the non-dimensional mass of the tube including the core, and is given by

$$\overline{m} \equiv \frac{m}{\rho L^3} = 4\overline{b}\overline{t} + \overline{\rho}_c(\overline{b} - \overline{t})^2. \tag{16}$$

Minimum mass designs, consistent with the practical constraints [Eqs. (1) and (2)], are obtained for two sets of assumptions, as follows.

Optimisation sub-task (i): vary $\overline{b}$ and $\overline{t}$ with the relative core density $\overline{\rho}_c$ held fixed at 0.1.

Optimisation sub-task (ii): vary $\overline{b}$, $\overline{t}$ and $\overline{\rho}_c$. The relative core density $\overline{\rho}_c$ is treated as a free variable within the range:

$$0 \leqslant \overline{\rho}_c \leqslant 0.25. \tag{17}$$

3.3. Topologies C, D, and E: a square hollow tube with sandwich walls

Next consider a hollow tube of square cross-section with sandwich panel walls. The core of the sandwich walls is a metal foam (Fig. 2c), a *square honeycomb* (Fig. 2d) or a *prismatic corrugated* core (Fig. 2e). Each solid facesheet has thickness t, the spacing between the mid-planes of the facesheets is d, and the centreline width of the square is b. Note that the total facesheet thickness of each wall is t for the foam-filled tube (topology B), while it is $2t$ for each sandwich panel of the hollow tube.

The mid-plane spacing d between the facesheets in topologies C to E is an additional geometrical variable. The full list of independent non-dimensionalised geometrical variables for these three topologies is now

$$\overline{b} \equiv b/L, \quad \overline{t} \equiv t/L, \quad \text{and} \quad \overline{d} \equiv d/L. \tag{18}$$

The non-dimensional mass for each of the topologies C to E reads

$$\overline{m} = \frac{m}{\rho L^3} = 4\overline{b}[2\overline{t} + \overline{\rho}_c(\overline{d} - \overline{t})]. \tag{19}$$

The normalised compliance $\overline{u}_m \equiv u_m EL/P$ is again given via Eqs. (14) and (15) with the dimensionless sectional properties of topologies C to E listed in Table 1. The dependence of core stiffness upon ρ_c varies from core to core, as summarised in Table 2 and as detailed below.

For topology C, the relative Young's modulus $\overline{E}_c$ of the foam core scales with $\overline{\rho}_c^2$, as stated by Eq. (7). *For topology D*, the square honeycomb core is characterised by its cell size l_c and cell wall thickness t_c, see Fig. 3a. The walls of the honeycomb core are aligned with the in-plane axes x_1 and x_2, while x_3 is the prismatic direction, as shown in Fig. 3a. The dependence of in-plane Young's modulus $\overline{E}_{11}^c$ and in-plane shear modulus $\overline{G}_{12}^c$ upon the relative density $\overline{\rho}_c$ of the core is taken from Gibson and Ashby (1997), Gu et al. (2001), and is stated as

$$\overline{E}_{11}^c = \overline{E}_{22}^c = \frac{E_{11}^c}{E} = \frac{1}{2}\overline{\rho}_c \tag{20}$$

$$\text{and} \quad \overline{G}_{12}^c = \frac{G_{12}^c}{E} = \frac{1}{16}\overline{\rho}_c^3, \tag{21}$$

$$\text{where} \quad \overline{\rho}_c = \frac{2t_c}{l_c}. \tag{22}$$

The detailed geometry of *topology E* is defined in Fig. 3b, along with a local co-ordinate frame x_i. The facesheets and the corrugated core are made from the same material, and the relative core density is

Table 2
Effective elastic moduli of the cores

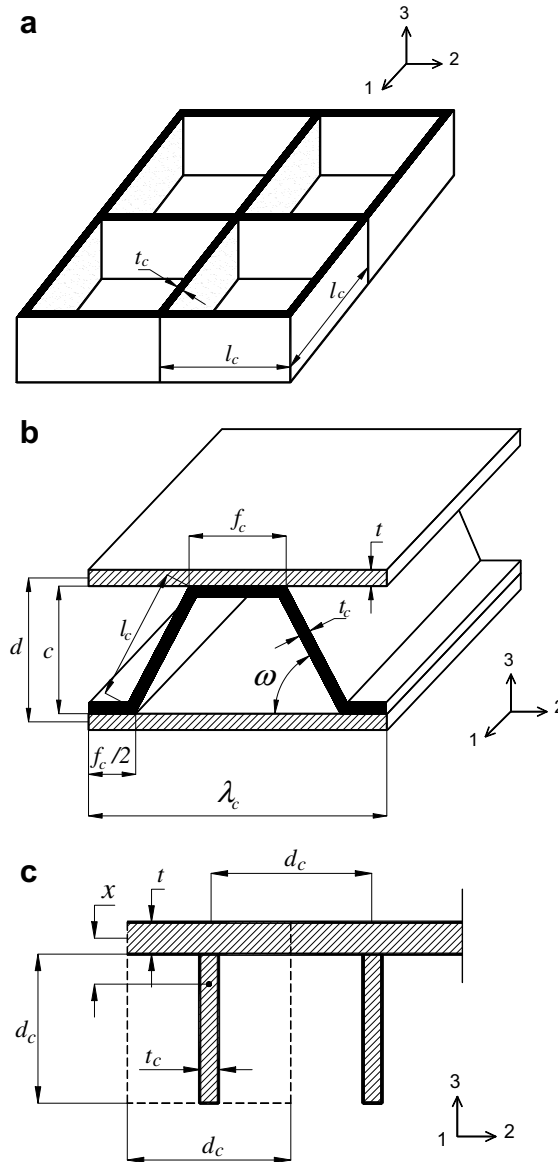| Cores	Relative Young's modulus $\overline{E}_{11}^c = E_{11}^c/E$	Relative shear modulus $\overline{G}_{12}^c = G_{12}^c/E$
Metal foam (Topologies B and C)	$\overline{\rho}_c^2$	$\frac{1}{2(1+\nu)}\overline{\rho}_c^2$
Square honeycomb (Topology D)	$\frac{1}{2}\overline{\rho}_c$	$\frac{1}{16}\overline{\rho}_c^3$
Corrugated core (Topology E)	$\overline{\rho}_c$	$\frac{0.648}{2(1+\nu)}\overline{\rho}_c$
Longitudinal ribs (Topology F)	$\overline{\rho}_c$	≈ 0

Fig. 3. Morphologies of (a) square honeycomb core (topology *D*); (b) a sandwich plate comprising a corrugated core (topology *E*); (c) a monolithic wall reinforced by a set of longitudinal equidistant ribs (topology *F*).

$$\overline{\rho}_{\rm c} = \frac{t_{\rm c}}{l_{\rm c}} \frac{(f_{\rm c}/l_{\rm c} + 1)}{(f_{\rm c}/l_{\rm c} + \cos\omega)\sin\omega} \tag{23}$$

in terms of the geometrical parameters shown in Fig. 3b. In order to reduce the number of geometrical degrees of freedom of the core, the core morphology is taken as

$$\omega = 45^0 \quad \text{and} \quad f_{\rm c}/l_{\rm c} = 0.5 \tag{24}$$

and Eq. (23) reduces to

$$\overline{\rho}_{\rm c} = 1.757 \frac{t_{\rm c}}{l_{\rm c}}. \tag{25}$$

The effective Young's modulus E_{11}^c of the corrugated core along the prismatic x_1-direction (see Fig. 3b) scales with $\overline{\rho}_c$ according to

$$\frac{E_{11}^c}{E} = \overline{\rho}_c. \tag{26}$$

A lower bound on the effective in-plane shear modulus G_{12}^c is derived by methods outlined by Gibson and Ashby (1997), giving

$$\overline{G}_{12}^c = \frac{0.648}{2(1+v)}\overline{\rho}_c. \tag{27}$$

(The upper bound value for G_{12}^c is only slightly above the lower bound but the expression is unwieldy). Two optimisation procedures are conducted for topologies C to E, as follows.

Optimisation sub-task (i): vary $\overline{b}$ and $\overline{t}$ with the relative density $\overline{\rho}_c$ held fixed at 0.1 and the aspect ratio $\overline{d}/\overline{t}$ equal to 10.

Optimisation sub-task (ii): vary $\overline{b}$, $\overline{t}$, $\overline{d}$, and $\overline{\rho}_c$. The relative density $\overline{\rho}_c$ is varied within the range:

$$0.05 \leqslant \overline{\rho}_c \leqslant 0.25 \tag{28a}$$

The upper and lower limits on $\overline{\rho}_c$ are due to practical limits on core manufacture. Similarly, $\overline{d}$ is allowed to vary over the practical range

$$\overline{t} \leqslant \overline{d} \leqslant \overline{b}/6. \tag{28b}$$

3.4. Topology F: a square hollow tube with monolithic walls reinforced internally by equi-spaced ribs

The hollow square tube is of overall width b, wall thickness t and stiffener-depth d_c, see Fig. 2f. Again, the non-dimensionalised geometrical variables are $\overline{b} \equiv b/L$, $\overline{t} \equiv t/L$ and $\overline{d}_c \equiv d_c/L$. The non-dimensional mass of the tube is

$$\overline{m} = \frac{m}{\rho L^3} = 4\overline{b}\overline{t} + 4\overline{d}_c(\overline{b} - \overline{t} - \overline{d}_c)\overline{\rho}_c. \tag{29}$$

A unit cell of the rib-reinforced walls and co-ordinate frame are given in Fig. 3c. The rib layer is considered as an equivalent homogeneous layer of effective density

$$\overline{\rho}_c = \frac{t_c}{d_c} \tag{30}$$

and of effective modulus

$$E_{11}^c = \overline{\rho}_c E. \tag{31}$$

The shear modulus G_{12}^c is negligible. Again two sets of calculations are performed, as follows:

Optimisation sub-task (i): vary $\overline{b}$ and $\overline{t}$ with the relative density $\overline{\rho}_c = 0.1$ and the aspect ratio $\overline{d}_c/\overline{t} = 10$.

Optimisation sub-task (ii): vary $\overline{b}$, $\overline{t}$, $\overline{d}_c$, and $\overline{\rho}_c$. The core density $\overline{\rho}_c$ varies as stipulated by Eq. (28a), while $\overline{d}_c$ varies over the range

$$0 \leqslant \overline{d}_c \leqslant \overline{b}/6. \tag{28c}$$

3.5. Results

The minimum mass and the optimised outer width of the beam with internal topologies A to F are shown in Figs. 4a and b as a function of the stiffness index $\overline{S}$ over the range 0–10^{-3}. The abscissa is taken as $\overline{S}^{1/2}$ in order to display the curves in the clearest manner.

Consider first the minimum mass design for topology A. No explicit optimisation step is needed and the unique relationship between $\overline{m}$ and $\overline{S}$ [Eqs. (6a) and (6b)] is given in Fig. 4a. This design has the highest mass of all topologies, and is thereby structurally inefficient.
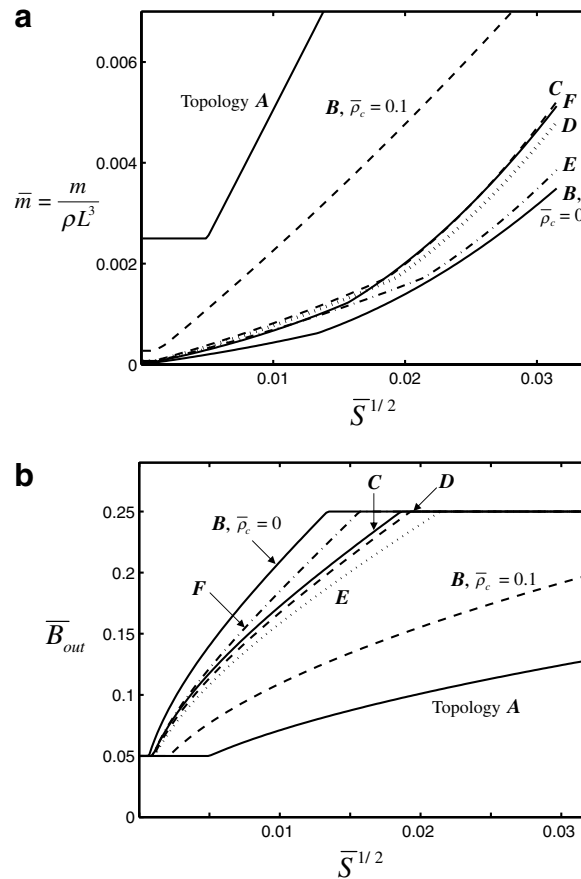
Fig. 4. (a) Minimum mass designs and (b) optimised outer widths of all topologies, Timoshenko beam theory. $\rho_c/\rho = 0.1$ and $d/t = 10$ for topologies C, D, and E. $\rho_c/\rho = 0.1$ and $d_c/t = 10$ for topology F.

The optimal design for topology B with $\overline{\rho}_c \equiv 0.1$ has a mass which is 50% less than that of the solid section (topology A). Upon further optimising with respect to $\overline{\rho}_c$, a much lighter design is obtained. The optimal design is achieved in the limit of $\overline{\rho}_c \rightarrow 0$, as shown in Fig. 4a. In fact, this is the lowest mass design of all the topologies considered.

Now the results of the optimisation task (i) for topologies C, D, and E. Recall that $\overline{\rho}_c \equiv 0.1$ and $\overline{d}/\overline{t} \equiv 10$, and optimisation is done with respect to $\overline{b}$ and $\overline{t}$. Topology E is the lightest and topology C is the heaviest, see Fig. 4a. However, the difference in mass is modest from one topology to the next. In the optimisation task (ii), $\overline{\rho}_c$ and $\overline{d}$ are treated as free variables. Minimum mass designs are achieved by taking the limit $\overline{d} \rightarrow \overline{t}$ such that no core is present in the sandwich walls. In this limit, the minimum masses for topologies C to E are identical to those already given for topology B with $\overline{\rho}_c = 0$.

Last, consider the square hollow tube with internal stringers, topology F. When an optimisation is conducted on $\overline{b}$ and $\overline{t}$, with $\overline{\rho}_c \equiv 0.1$ and $\overline{d}_c/\overline{t} \equiv 10$, the minimum mass design is intermediate between that for topologies C and E (with $\overline{\rho}_c \equiv 0.1$ and $\overline{d}/\overline{t} \equiv 10$). Upon treating $\overline{\rho}_c$ and $\overline{d}_c$ as free variables, the optimal design is achieved at $\overline{d}_c \rightarrow 0$, and the limit of a hollow tube with solid walls (topology B with $\overline{\rho}_c = 0$) is again recovered.

Recall that upper and lower practical constraints on $\overline{B}_{out}$ have been imposed via Eq. (1) for each topology. At low $\overline{S}$, the optimal value of $\overline{B}_{out}$ is 0.05 for all topologies. For topologies B to F, $\overline{B}_{out}$ then increases with increasing $\overline{S}$ until it saturates at the upper limiting value of $\overline{B}_{out} = 0.25$ (the 'stubby beam limit'), see Fig. 4b. In contrast, the beam of solid cross-section, topology A, shows only a modest sensitivity of $\overline{B}_{out}$ to $\overline{S}$.

The above analysis is valid when the mid-span loading is introduced in a sufficiently distributed manner that Timoshenko beam theory applies. In practice, this is difficult to achieve, and the additional compliance

due to load introduction over a finite patch is now explored. We shall show that the optimum topology changes due to this additional compliance.

4. Optimisation using the coupled theory of Timoshenko beam theory and the local compliance associated with patch loading

The local compliance near the central loading patch is now combined with the macroscopic beam compliance according to Timoshenko beam theory in order to obtain analytical expressions for the total deflection at the central point of the upper surface. While the effect of local compliance upon the overall response is negligible for the solid square beam (topology A), the other topologies have significant local compliance at the central loading patch. The local response is analysed in detail for the foam-filled tube (topology B), and is summarised in less detail for the remaining topologies. Minimum mass designs are again obtained for each topology.

4.1. Structural response of topology B

4.1.1. Analytical prediction

In addition to the macroscopic bending and shearing deflection of the whole tube, local bending of the upper solid facesheet occurs under the localised load at mid-span. Studies by Thomsen (Thomsen, 1993; Zenkert, 1995) on sandwich beams and plates under localised loads suggest that the total displacement and the total in-plane stresses of the loaded face is adequately approximated by the superposition of the global solution (obtained by classical beam theory) and the approximate local solution.

In the present study, the total deflection u_t is taken to be the sum of the macroscopic deflection u_m (according to Timoshenko beam theory) and the local deflection of the loaded facesheet at the central point of the upper surface, u_l

$$u_t = u_m + u_l. \tag{32}$$

It is assumed that the macroscopic deflection u_m is an adequate approximation for the deflection of the neutral axis of the beam cross-section at mid-span. For example, for topology B, the deflection u_A of the point A on the neutral axis shown in Fig. 5a is given by u_m. In contrast, the loaded face of the beam undergoes an additional deflection u_l. For topology B it is assumed that the deflection of the point B at the centre of the top surface, and under the loading patch (see Fig. 5a), is given by $u_B = u_A + u_l$.

The macroscopic deflection u_m has already been discussed in Section 3.2 and is given by Eq. (3). It is assumed that the local deflection of the upper solid facesheet equals the bending deflection of a simply supported square solid plate of width b, resting upon an elastic foundation (the foam core), and subjected to a transverse pressure $q = P/w^2$ uniformly distributed over the central patch area, see Fig. 6a. The Winkler foundation model is used to describe the support of the plate by the core. This problem has already been discussed by Timoshenko and Woinowsky-Krieger (1970), and Navier's solution is

$$u_{\text{plate}} = \sum_{m=1}^{\infty} \sum_{n=1}^{\infty} \frac{a_{mn}}{\frac{\pi^4 D_f}{(1-v^2)} \left(\frac{m^2+n^2}{b^2}\right)^2 + k} \sin \frac{m\pi x_1}{b} \sin \frac{n\pi x_2}{b}, \tag{33}$$

where

$$a_{mn} = \frac{16P}{\pi^2 mnw^2} \sin \frac{m\pi}{2} \sin \frac{n\pi}{2} \sin \left(\frac{m\pi}{2} \frac{w}{b}\right) \sin \left(\frac{n\pi}{2} \frac{w}{b}\right) \tag{34}$$

and

$$D_f = \frac{Et^3}{12} \tag{35}$$

is the flexural rigidity of the facesheet. Here, k is the elastic foundation modulus of the core in the transverse direction. This modulus is expressed in accordance with Thomsen (1993) and Vlasov and Leont'ev (1960), as

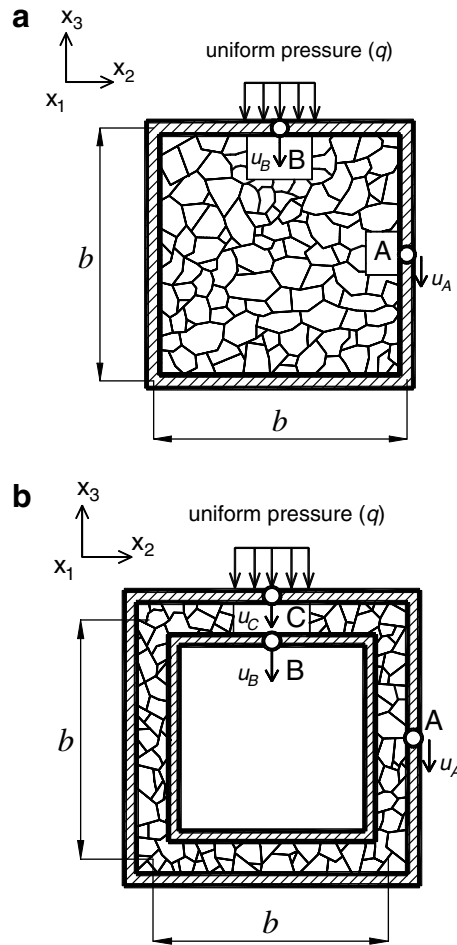$$k = \frac{E_0 \gamma}{b(1-v_0^2)} \psi, \tag{36}$$

Fig. 5. (a) Deflections at selected locations of the cross-section of the foam-filled tube (topology *B*). The displacement of point A equals the macroscopic deflection, while the displacement of point B equals the total deflection. (b) Deflections at selected locations of the hollow sandwich-walled tube (topology *C*). The macroscopic deflection, local deflection, and the total deflection are given by the deflections of points A, B, and C, respectively.

where

$$E_0 = \frac{E_c}{(1 - v_c^2)}, \quad v_0 = \frac{v_c}{(1 - v_c)},$$

$$\psi = \frac{\sinh \phi \cosh \phi + \phi}{\sinh^2 \phi}, \quad \phi = \frac{2\gamma c}{b}. \tag{37}$$

The thickness c of the core layer (i.e. the elastic foundation depth) is taken to be

$$c = b - t. \tag{38}$$

The constant γ dictates the elastic properties of the foundation and gives the decay rate of displacement over the foundation depth (Vlasov and Leont'ev (1960)). Thomsen (1993) chose $\gamma = 1.5$ in their study of a simply supported sandwich plate with a PVC-foam core. In the present study, we shall adopt the value

$$\gamma = 2.5 \tag{39}$$

in order to give closer agreement with the finite element results (shown later in Fig. 7).
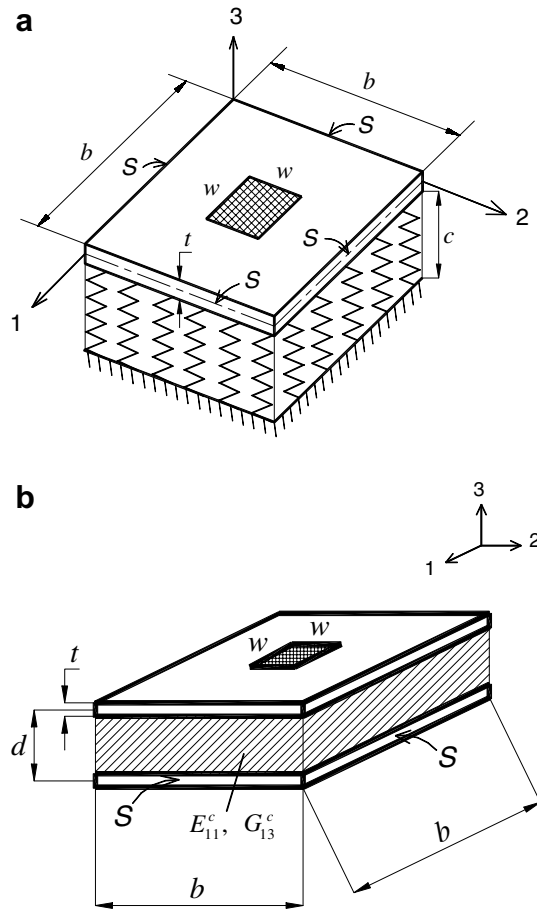
Fig. 6. (a) A square, simply supported (S) monolithic solid plate on an elastic foundation under uniform pressure over the central area (w × w) of the plate. (b) A square, simply supported (S) isotropic sandwich plate under uniform pressure over the central area (w × w) of the plate.

The local deflection u_l in Eq. (33) is taken to be the central deflection of the plate (u_{plate} at $x_1 = x_2 = b/2$). The non-dimensional deflection $\overline{u}_l$ reads from Eqs. (33)–(37) as

$$\overline{u}_l \equiv \frac{u_l E L}{P} = \frac{16}{\pi^2 \overline{w}^2} \sum_{m=1}^{\infty} \sum_{n=1}^{\infty} \frac{\sin^2\left(\frac{m\pi}{2}\right) \sin^2\left(\frac{n\pi}{2}\right) \sin\left(\frac{m\pi}{2}\frac{\overline{w}}{\overline{b}}\right) \sin\left(\frac{n\pi}{2}\frac{\overline{w}}{\overline{b}}\right)}{mn\left\{\frac{\pi^4 \overline{t}^3}{12(1-v^2)}\left(\frac{m^2+n^2}{\overline{b}^2}\right)^2 + \frac{\gamma\psi}{\overline{b}}\frac{(1-v_c)\overline{E}_c}{(1+v_c)(1-2v_c)}\right\}}. \tag{40}$$

Recall that $\overline{w} \equiv w/L = 0.05$ is the assumed dimensionless width of the loading patch. For the foam core, $\overline{E}_c = \overline{\rho}_c^2$ and $v_c = 0.3$. The overall non-dimensional stiffness now reads $\overline{S} = 1/(\overline{u}_m + \overline{u}_l)$, where $\overline{u}_m$ and $\overline{u}_l$ are given by Eqs. (14) and (40), respectively.

4.1.2. Accuracy of analytical predictions: comparison with selected finite element simulations

The commercial finite element software ABAQUS (version 6.4, 2004) has been used to assess the accuracy of the analytical predictions. The three-dimensional structural response of the foam-filled tube (topology B) is calculated for the three-point bending described in Fig. 1. The solid facesheets are modelled using 4-noded shell elements with reduced integration (element type S4R in the ABAQUS notation), while the foam core is simulated by 8-noded linear brick elements with reduced integration (element type C3D8R). The facesheets are tied to the core by tie constraints. Both the facesheets and foam core are meshed such that 12 elements exist
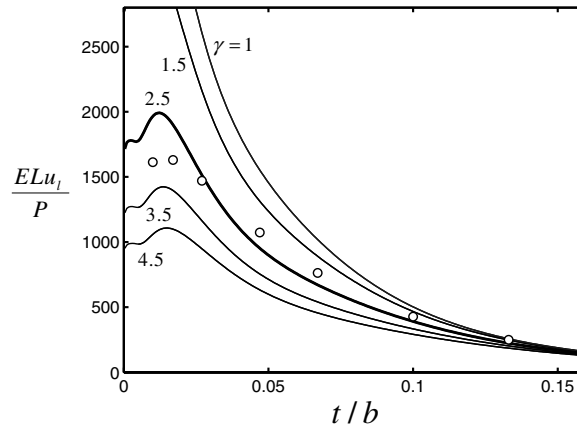
Fig. 7. The local compliance of topology B with $\bar{\rho}_c = 0.1$, for selected values of γ. The analytical predictions, as given by the solid curves, are calibrated against the finite element predictions, as shown by discrete data points.

along the width and depth directions, and 108 elements exist along the tube span. Numerical simulations are made for $H/L = 0.175$, $b/L = 0.15$, and $w/L = 0.05$. The facesheets and foam core share a Poisson ratio of $v = v_c = 0.3$, while the foam core has a Young's modulus of $E_c = 0.01E$.

Consider first the finite element prediction for the local compliance ELu_l/P of the foam-filled tube as a function of t/b, see Fig. 7. The compliance drops with increasing t/b due to the increasing bending stiffness of the tube wall. The figure includes the analytical prediction [Eq. (40)] for selected values of the constant factor γ. The value for γ in the elastic foundation model is chosen to match the full FE solution. It is apparent that an appropriate choice for γ is 2.5, as already asserted above. We employ this value hereafter.

Finite element predictions for the local and macroscopic compliances are plotted as a function of normalised wall thickness t/b in Fig. 8a for a hollow tube and in Fig. 8b for a foam-filled tube. The figures include the analytical predictions for comparison purposes. Consider first the hollow tube with monolithic walls, Fig. 8a. The dimensionless macroscopic and local deflections are given analytically by Eqs. (14) and (40), with the core Young's moduli E_c set to zero. The local deflection scales with t according to t^{-3}, while the macroscopic deflection is proportional to t^{-1}. When the ratio t/b is small, say 0.01, the local deflection is about two orders of magnitude greater than the macroscopic deflection; alternatively, when t/b is large, say above 0.1, the macroscopic deflection dominates.

The presence of a foam core in the tube enhances both the macroscopic and local stiffnesses, compare Figs. 8a and b. For example, when the facesheet is very thin ($t/b = 0.01$), the presence of the foam core reduces the local deflection by a factor of about 350. We conclude that the agreement between the analytical predictions and the FE predictions are adequate for our purposes.

4.2. Structural response of topology C

The total mid-span deflection u_t for topology C is taken as the sum of the macroscopic deflection and the local deflection, as stated by Eq. (32). Recall that the macroscopic deflection u_m (deflection of point A, Fig. 5b) is defined by Eq. (3). The deflection of the inner sandwich wall at point B of Fig. 5b equals u_m plus the deflection u_{sp} of a simply supported square sandwich plate of width b subjected to a uniform pressure $q = P/w^2$ over a central patch of the upper facesheet, see Fig. 6b. Thus the deflection of point B is $u_B = u_m + u_{sp}$. The outer loaded face of the sandwich wall (point C of Fig. 5b) deflects by a value $u_C \equiv u_t$ equal to u_B plus an additional contribution u_{ind} from local indentation of the loaded upper facesheet upon an elastic foundation
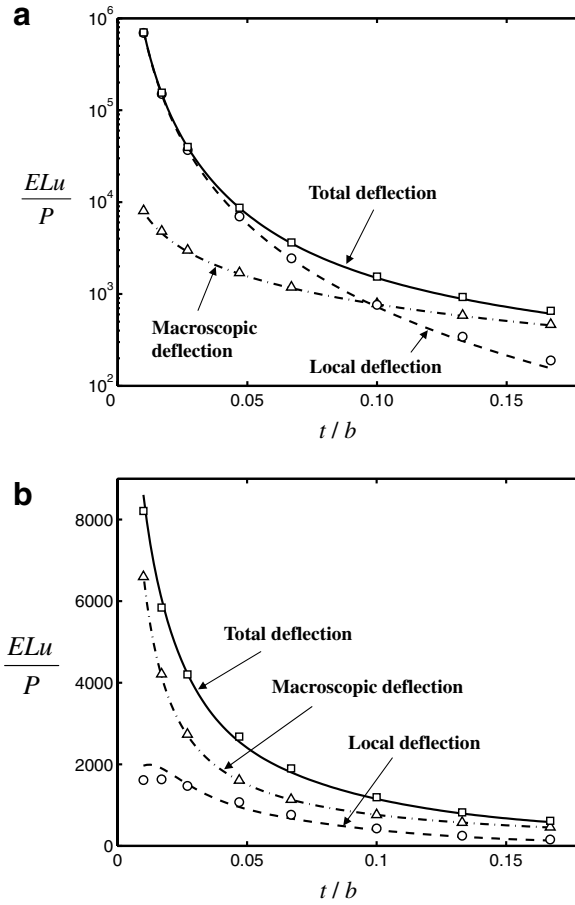
$$u_C = u_B + u_{ind}$$
$$= u_m + u_{sp} + u_{ind}. \tag{41}$$

Fig. 8. Compliances of (a) hollow solid-walled tube (topology B with $\overline{\rho}_c = 0$), and (b) foam-filled tube (topology B with $\overline{\rho}_c = 0.1$). Non-dimensional resulted deflections are plotted as functions of ratio t/b. The lines are the analytical predictions, and the symbols are the finite element results.

Thus, the local deflection is taken as $u_l = u_{sp} + u_{ind}$. The analytical models used to calculate u_{sp} and u_{ind} are now described. It is assumed that the deflection u_{sp} is adequately given by the central deflection of a simply supported sandwich plate, of width b, subjected to a uniform pressure $q = P/w^2$ as sketched in Fig. 6b. The cross-section of the sandwich plate has a *flexural rigidity D* and a *shearing rigidity D_Q*. The dimensionless formula for u_{sp} is given in Eq. (B.1) of Appendix B.

The local indentation u_{ind} is taken as the bending deflection of a simply supported square solid plate of width b upon an elastic foundation. The formula (40) is again used, but now for topology C, the thickness c of the core layer is

$$c = d - t. \tag{42}$$

The constant factor $\gamma = 2.5$ remains unchanged. The normalised overall stiffness is $\overline{S} = 1/(\overline{u}_m + \overline{u}_{sp} + \overline{u}_{ind})$ with $\overline{u}_m$, $\overline{u}_{sp}$ and $\overline{u}_{ind}$ given by Eqs. (14), (B.1), and (40), respectively.

4.3. Optimisation of topologies A, B, and C

Return now to the minimum mass design of a beam of specified stiffness S with the local compliance taken into account. For both topologies B and C, the independent geometrical variables are given by Eqs. (13) and (18), respectively, and the objective function in the form of the tube mass is given by Eqs. (16) and (19), respec-

tively. The additional practical constraints, Eqs. (1), (2), and (17) for topology B and Eqs. (1), (2), and (28a), (28b) for topology C, are included in the optimisations. Two optimisation tasks are again performed for both topologies B and C.
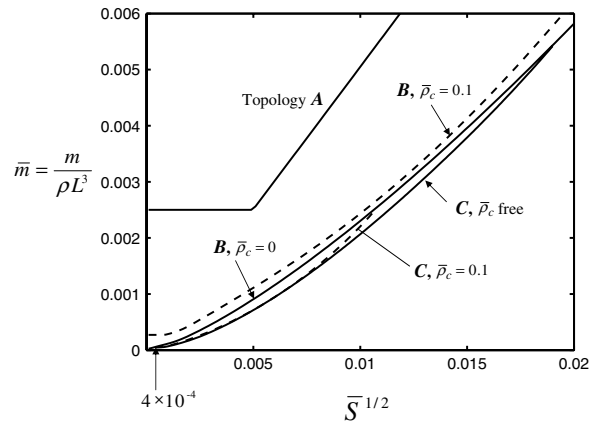

Fig. 9. Minimum mass designs of topology A, topology B ($\bar{\rho}_c = 0.1$ and $\bar{\rho}_c = 0$), and topology C ($\bar{\rho}_c = 0.1$ and $\bar{\rho}_c$ free) using the coupled theory.
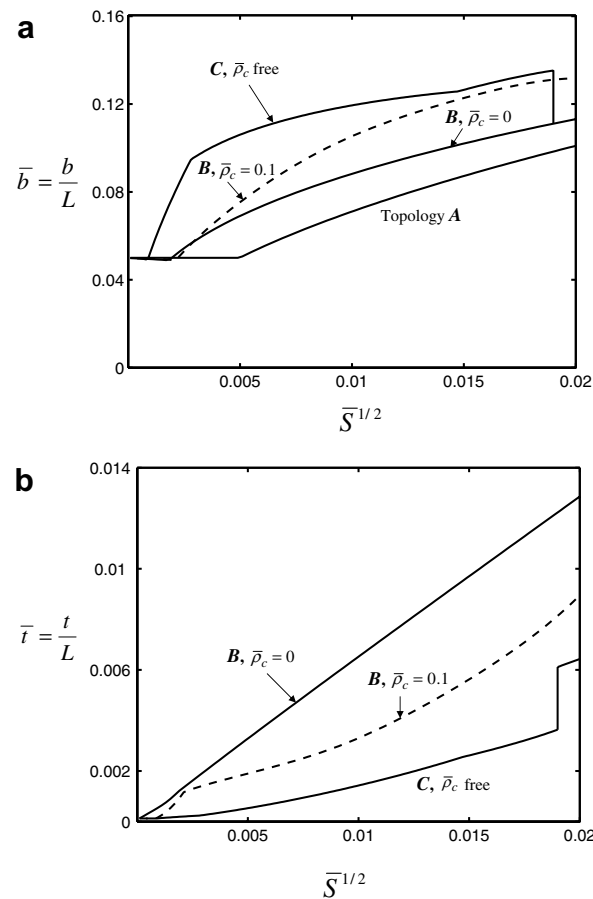

Fig. 10. (a) Optimised beam width $\bar{b}$ and (b) optimised facesheet thickness $\bar{t}$ of topology A, topology B ($\bar{\rho}_c = 0.1$ and $\bar{\rho}_c = 0$), and topology C (sub-task (ii)) using the coupled theory.

Optimisation sub-task (i): The relative core density $\overline{\rho}_c$ is held fixed at 0.1. $\overline{b}$ and $\overline{t}$ are free independent variables for topology B, while $\overline{b}$, $\overline{t}$, and $\overline{d}$ are allowed to vary for topology C.

Optimisation sub-task (ii): $\overline{b}$, $\overline{t}$, and $\overline{\rho}_c$ are allowed to vary for topology B, whilst $\overline{b}$, $\overline{t}$, $\overline{d}$, and $\overline{\rho}_c$ are free variables for topology C. The relative core density $\overline{\rho}_c$ is constrained to lay within the range 0–0.25 for topology B, and within 0.05–0.25 for topology C.

Results

Minimum mass designs are shown in Fig. 9 for both optimisation tasks (i) and (ii). For the solid square beam (topology A) the local compliance is taken to vanish, and the optimised results are those already given by Eqs. (6) from Timoshenko beam theory. Topology A remains the heaviest topology. For the tubular topologies B and C, the finite local compliance leads to a higher mass than that predicted by Timoshenko beam theory for these topologies.

Consider topology B in more detail. When $\overline{\rho}_c$ is held fixed at 0.1, the optimised foam-filled tube is much lighter than the solid beam, and is slightly heavier than the hollow tube with monolithic walls, see Fig. 9. When $\overline{\rho}_c$ is allowed to vary, the minimum mass is achieved at $\overline{\rho}_c \to 0$. This conclusion is consistent with that obtained
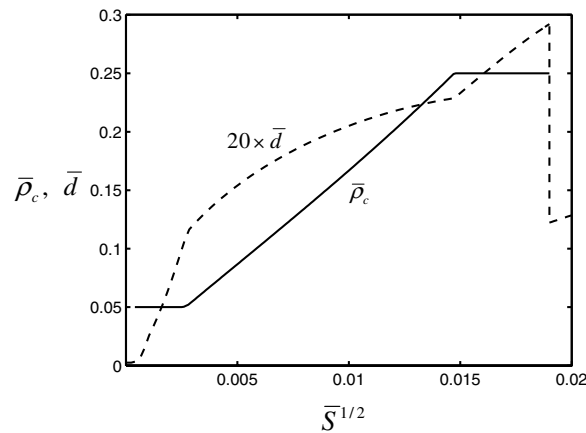

Fig. 11. Optimised mid-plane spacing $\overline{d}$ between the facesheets and optimised relative core density $\overline{\rho}_c$ of topology C (sub-task (ii)), coupled theory.
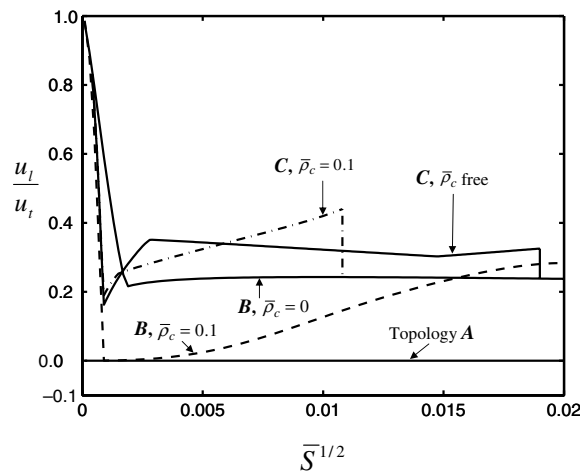

Fig. 12. Ratio of the local deflection to the total deflection of topology A, topology B ($\overline{\rho}_c = 0.1$ and $\overline{\rho}_c = 0$), and topology C ($\overline{\rho}_c = 0.1$ and $\overline{\rho}_c$ free), coupled theory. Results are given for the minimum mass designs.

in Section 3 for Timoshenko beam theory: the hollow tube is the more efficient than the foam-filled tube. The optimised values of $\bar{b}$ and $\bar{t}$ for topology B are plotted as a function of $\bar{S}^{1/2}$ in Figs. 10a and b.

Next consider topology C with the optimisation conducted with $\bar{\rho}_c$ held fixed at 0.1 (optimisation task (i)). For low values of stiffness index, $\bar{S}^{1/2} < 4 \times 10^{-4}$, the optimal design of topology C has the feature that the core of the sandwich walls vanishes, $d \to t$. In this limit the topology reduces to that of a hollow monolithic tube, which is identical to topology B with $\bar{\rho}_c \equiv 0$, see Fig. 9. At intermediate $\bar{S}$, such that $4 \times 10^{-4} \leqslant \bar{S}^{1/2} \leqslant 0.011$ the optimal design for topology C in optimisation task (i) has sandwich walls with a core of finite thickness, $d > t$. This topology has a lower mass than that of a hollow tube with monolithic walls (topology B with $\bar{\rho}_c \equiv 0$). At $\bar{S}^{1/2} > 0.011$, the optimal design for topology C is again the hollow monolithic tube.

Results are now given for topology C with $\bar{\rho}_c$ allowed to vary over the range $0.05 \leqslant \bar{\rho}_c \leqslant 0.25$ (optimisation task (ii)). At low $\bar{S}$, such that $\bar{S}^{1/2} < 4 \times 10^{-4}$, the optimal topology C is again the hollow monolithic tube. Over a wide range of $\bar{S}$, such that $4 \times 10^{-4} \leqslant \bar{S}^{1/2} \leqslant 0.019$, the topology C has sandwich walls of finite core thickness and has a lower mass than that of topology C with $\bar{\rho}_c$ held fixed at 0.1, recall Fig. 9. The two cases coincide at $\bar{S}^{1/2} = 0.006$; for this value of $\bar{S}$ the optimal choice of $\bar{\rho}_c$ is 0.1 and the solution for optimisation task (ii) gives the same result as that for optimsation task (i) where $\bar{\rho}_c$ is held fixed at 0.1. At $\bar{S}^{1/2}$ above 0.019, the optimal topology for C with variable $\bar{\rho}_c$ coincides with that of a hollow monolithic tube: in topology C the sandwich walls have a core of zero thickness, $d \to t$. The geometry of topology C and the value of $\bar{\rho}_c$ to minimise the tube mass in sub-task (ii) are summarised in Figs. 10 and 11. For $\bar{S}$ in the intermediate range, we find that $\bar{\rho}_c$, $\bar{b}$, $\bar{t}$, and $\bar{d}$ all increase with $\bar{S}$.

Recall that the coupled theory asserts that the total deflection u_t is the algebraic sum of the macroscopic deflection u_m and a local deflection u_l due to bending of the loaded wall of the tube. The local deflection u_l is a significant fraction of u_t for topologies B and C, as shown in Fig. 12. Also, for both topologies B and C, u_l/u_t increases sharply with diminishing $\bar{S}$, for $\bar{S}^{1/2} < 0.002$. This feature is due to the fact that the lower constraint on $\bar{B}_{out}$ is active for $0 < \bar{S}^{1/2} < 0.002$: recall that $\bar{B}_{out}$ is constrained to not fall below 0.05, see Fig. 10a. Consequently, the sandwich walls have a large span and possess a large local compliance.

4.4. Optimisation of topologies D, E, and F using the coupled theory

The coupled theory is now applied to find the minimum mass for the beam with topologies D to F. Analytical expressions for the local compliance for topology D are included in Appendix B and for topologies E and F in Appendix C. Minimum mass designs are obtained for each topology, with $\bar{\rho}_c$ treated as a free variable together with the other geometrical variables. The results for the minimum mass of all these structures are presented in Fig. 13 and include those taken from Fig. 9 for a solid square beam (topology
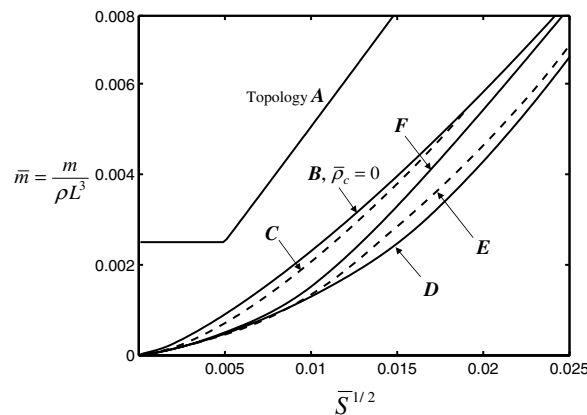

Fig. 13. Minimum mass designs of topology A, topology B (with $\bar{\rho}_c = 0$), and topologies C to F (with $\bar{\rho}_c$ free) using the coupled theory.

A), for a hollow tube with monolithic walls (topology *B* with $\overline{\rho}_c \equiv 0$) and for topology *C* (with $\overline{\rho}_c$ treated as a free variable).

Recall that the lattice *square honeycomb* and *corrugated* cores are superior to the other cores in the sense that their moduli (with the exception of the in-plane shear modulus of square honeycomb and the local shearing stiffness of the corrugated core) scale linearly with the relative density of the core. Consequently, the hollow tube with sandwich walls (topologies *D* and *E*) have the lowest mass of all topologies considered. For low to modest value of stiffness index $\overline{S}$, the relative ranking of the topologies is insensitive to the stiffness index $\overline{S}$: the preferred choice for topology on the basis of minimum mass is *D*, *E*, *F*, *C*, *B*, and last the solid beam *A*, see Fig. 13.

5. The significance of the inner cavity on the optimal design

In practical design, the dimension of the inner core of a structural tube (such as the moving head of a milling machine) is constrained. The tube must contain internal components such as electrical and hydraulic cables, motors and spindles. Consequently, the dimensionless inner width $\overline{B}_{in} \equiv B_{in}/L$ of the hollow tube must exceed a pre-defined non-dimensional width $\overline{B}_0 \equiv B_0/L$. The inner dimension $\overline{B}_{in}$ depends upon $(\overline{b}, \overline{t}, \overline{d}, \overline{d}_c)$ according to

$$\overline{B}_{in} = \overline{b} - \overline{t} \geqslant \overline{B}_0, \quad \text{topology } B \text{ with } \overline{\rho}_c \equiv 0,$$
$$\overline{B}_{in} = \overline{b} - \overline{t} - \overline{d} \geqslant \overline{B}_0, \quad \text{topologies } C \text{ to } E,$$
$$\text{and} \quad \overline{B}_{in} = \overline{b} - \overline{t} - 2\overline{d}_c \geqslant \overline{B}_0, \quad \text{topology } F. \tag{43}$$

The significance of this additional constraint on minimum mass design is shown in Fig. 14, in which the inner width has been constrained to exceed

$$\overline{B}_{in} \geqslant 0.15. \tag{44}$$

It is concluded from Fig. 14 that internal stiffeners attached to the walls of the tube are structurally inefficient: the minimum mass trajectory for topology *F* is identical to that of the hollow monolithic-walled tube (i.e. topology *B* with $\overline{\rho}_c = 0$). The local deflection contribution to the total deflection of the hollow tube with solid walls (topology *B* with $\overline{\rho} = 0$) is shown in Fig. 15. The active constraint on $\overline{B}_{in}$ leads to large local compliances for topology *B* (and *F*). It is concluded that sandwich construction for the tube walls is advantageous. The lowest mass design is achieved by topology *D*, followed by *E* and *C*, recall Fig. 14.

The accuracy of the analytical predictions for topology *B* with $\overline{\rho}_c \equiv 0$ and the constraint on $\overline{B}_{in}$ imposed is explored in Figs. 14 and 15. Finite element results are shown for the optimal geometries as deduced by
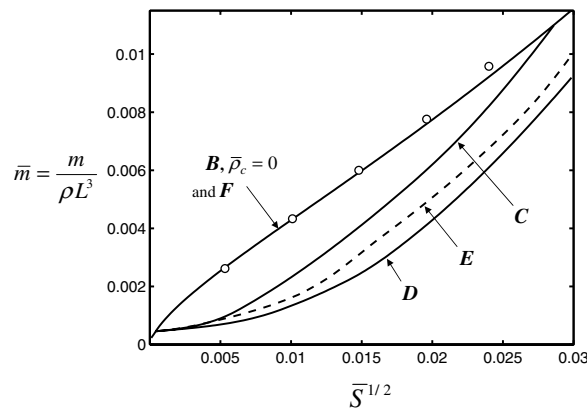

Fig. 14. Minimum mass designs of all hollow structures: topology *B* (with $\overline{\rho}_c = 0$), and topologies *C* to *F* (with $\overline{\rho}_c$ free) using the coupled theory with the inner width constraint $B_{in} \geqslant 0.15L$ imposed. The discrete points denote the finite element results for topology *B*, with $\overline{\rho}_c = 0$.
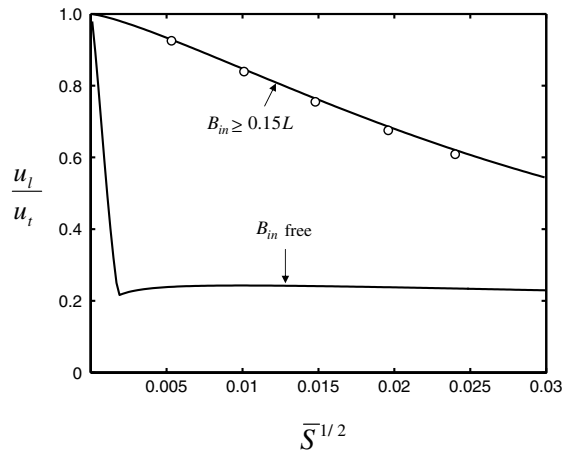
Fig. 15. Ratio of the local deflection to the total deflections of topology B ($\overline{\rho}_c = 0$) with and without constraint on the inner width, coupled theory. The finite element results are shown by discrete data points for the constrained case, $B_{in} \geqslant 0.15L$.

the optimisation analysis using the coupled theory. It is clear that the analytical formulae for topology B suffice.

6. Concluding remarks

In this paper, minimum mass designs are obtained as a function of required stiffness index for beams with various internal topologies in three-point bending. It is shown that significant local deflections of the tube walls occur near to the central loading patch. The analytical predictions of both macroscopic and local compliances are validated by numerical results for a foam-filled tube and a hollow tube with foam-cored sandwich walls. This theoretical analysis is generalised for the remaining structures: hollow tubes with sandwich walls comprising different lattice cores (*square honeycomb* and *corrugated*), and a hollow tube with rib-reinforced monolithic walls.

The optimum topology depends upon whether local and global compliances are considered or not in the analysis. When only macroscopic bending is considered using Timoshenko beam theory, the square hollow tube with monolithic walls (topology B with $\overline{\rho} \equiv 0$) is the lightest structure for any given stiffness index. When the local compliance of the tube walls is included in the analysis, sandwich construction for the tube walls leads to reduced mass for an intermediate range of stiffness index. Hollow square tubes with sandwich walls using square honeycomb core (topology D) and corrugated core (topology E) have the lowest mass. The optimised hollow sandwich-walled tube using metal foam (topology C) is competitive with the conventional hollow tube using stiffened-walls (topology F). Upon imposing additional constraints, such as a constraint on the inner tube width, the relative performance of various topologies changes. For the constraint adopted here on the inner width of the hollow tube, sandwich wall construction is the appropriate choice, and outperforms the use of internal stringer reinforcement.

Acknowledgements

Appendix A. Shear coefficient of a sandwich beam

Consider first a monolithic beam. The slope of the deflection curve of the beam due to shear du_s/dx_1 is approximately equal to the shear strain at the neutral axis of the cross-section, γ^{max}, see for example, Timoshenko and Gere (1972). Thus, the beam deflection due to shear is calculated by making the identity

$$\frac{du_s}{dx_1} \equiv \gamma^{max}. \tag{A.1}$$

The maximum shear strain γ^{max} scales with the shear force V on the beam. We write

$$\gamma^{max} = \alpha_s \frac{V}{GA}, \tag{A.2}$$

where G is the shear modulus, A is the beam cross-section and α_s is a numerical factor (or *shear coefficient*). Note that α_s is, by definition, the ratio of maximum shear strain at the neutral axis to the average shear strain. The quantity GA/α_s is the *shearing rigidity* of the beam.

An alternative procedure for determining the shear deflection of the beam is to employ the principle of virtual work. The final result for du_s/dx_1 can be written in the form

$$\frac{du_s}{dx_1} \equiv f_s \frac{V}{GA}, \tag{A.3}$$

where f_s is the *form factor* for shear, Timoshenko and Gere (1972). This method gives a more accurate value for the shear deflection. However, the algebraic calculation of f_s is lengthy, and the simpler approach of determining α_s is preferred in the present study. The transverse shear effect is practically small so the results are relatively insensitive to the use of α_s instead of f_s.

Now consider the representative example of a rectangular beam, as shown in Fig. A.1a. Simple beam theory assumes that the shear stress is distributed uniformly across the width of the beam, and the maximum shear stress γ^{max} at the neutral axis is related to the shear force V on the beam cross-section by

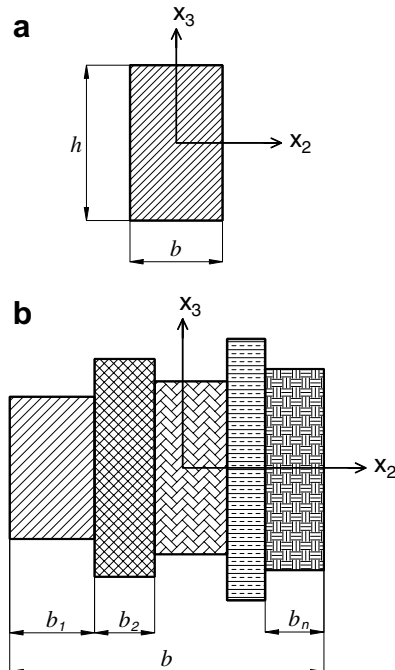Fig. A.1. Cross-sections of (a) a rectangular monolithic beam, and (b) a symmetric sandwich beam.

$$\gamma^{\max} = \frac{VQ}{GIb}. \tag{A.4}$$

Here, Q is the first moment about the neutral axis of the portion of the cross-sectional area above the neutral axis, I is the second moment of the cross-sectional area, and b is the width of the rectangular beam. The average shear stress over the cross-section $\bar{\tau}$ reads $\bar{\tau} = V/A$, and the average shear strain $\bar{\gamma}$ is

$$\bar{\gamma} = \frac{\bar{\tau}}{G} = \frac{V}{GA}. \tag{A.5}$$

The shear coefficient α_s reads

$$\alpha_s \equiv \frac{\gamma^{\max}}{\bar{\gamma}} = \frac{QA}{Ib} = 1.5. \tag{A.6}$$

Next, consider a symmetric sandwich structure comprising n layers as shown in Fig. A.1b. The layers bend together in the x_1–x_3 plane, and share the same bending curvature κ. Consequently, the bending moment on each layer scales with the bending rigidity as

$$M_i = E_i I_i \kappa, \quad i = 1 \text{ to } n, \tag{A.7}$$

where M_i, E_i, I_i are the moment, Young's modulus and second moment of the cross-sectional area of the ith layer, respectively. With $M \equiv \sum_{i=1}^{n} M_i$ as the total bending moment, and the *equivalent flexural rigidity* defined by $(EI)_{\mathrm{eq}} \equiv \sum_{i=1}^{n} E_i I_i$, we obtain

$$M_i = \frac{E_i I_i}{(EI)_{\mathrm{eq}}} M. \tag{A.8}$$

Equilibrium dictates that the shear force on the ith layer is $V_i = \mathrm{d}M_i/\mathrm{d}x_1$ so that

$$V_i = \frac{E_i I_i}{(EI)_{\mathrm{eq}}} V. \tag{A.9}$$

Here, $V = \mathrm{d}M/\mathrm{d}x_1 = \sum_{i=1}^{n} V_i$ is the total shear force on the cross-section. The shear stress within layer i on the neutral plane of the composite beam is

$$\tau_i = \frac{V_i Q_i}{I_i b_i} = \frac{V}{(EI)_{\mathrm{eq}}} \frac{E_i Q_i}{b_i}, \tag{A.10}$$

where Q_i is the first moment of layer i about the neutral axis of the beam, and b_i is the width on the neutral plane.

The *total line shear force* at the neutral axis of the whole cross-section is defined by

$$\hat{V} \equiv \sum_{i=1}^{n} \tau_i b_i = \frac{V(EQ)_{\mathrm{eq}}}{(EI)_{\mathrm{eq}}} \quad \text{where } (EQ)_{\mathrm{eq}} \equiv \sum_{i=1}^{n} E_i Q_i. \tag{A.11}$$

Assume that the *line shearing rigidity* at the neutral axis is given by Voigt bound

$$(Gb)_{\mathrm{eq}} \equiv \sum_{i=1}^{n} G_i b_i. \tag{A.12}$$

Then, the *line maximum shear strain* $\hat{\gamma}$ over the width $b = \sum_{i=1}^{n} b_i$ of the whole cross-section at the neutral axis is

$$\hat{\gamma} \equiv \frac{\hat{V}}{(Gb)_{\mathrm{eq}}} \tag{A.13}$$

and upon making use of Eq. (A.11) it reads

$$\hat{\gamma} = \frac{V(EQ)_{\mathrm{eq}}}{(EI)_{\mathrm{eq}}(Gb)_{\mathrm{eq}}}. \tag{A.14}$$

The average shear strain over the whole cross-sectional area is

$$\bar{\gamma} \equiv \frac{V}{(GA)_{\mathrm{eq}}}, \tag{A.15}$$

where $(GA)_{\mathrm{eq}} \equiv \sum_{i=1}^{n} G_i A_i$. The shear coefficient follows as

$$\alpha_s \equiv \frac{\hat{\gamma}}{\bar{\gamma}} = \frac{(EQ)_{\mathrm{eq}}}{(EI)_{\mathrm{eq}}} \frac{(GA)_{\mathrm{eq}}}{(Gb)_{\mathrm{eq}}}. \tag{A.16}$$

Appendix B. Local deflections of topologies *C* and *D*

As stated in Section 4.2, the local deflection of the loaded upper sandwich wall of topologies *C* and *D* is assumed to equal the deflection of a simply supported square sandwich plate of width *b*, subjected to a uniform pressure $q = P/w^2$ distributed over a central patch of the upper facesheet, see Fig. 6b. This local deflection u_l comprises the bending and shearing deflection of the whole sandwich plate u_{sp}, and an additional local indentation of the loaded upper facesheet u_{ind} upon an elastic foundation (the core within the upper sandwich wall).

B.1. Local bending and shearing deflection u_{sp}

The stiffness of a sandwich plate subjected to lateral loading is discussed by Allen (1969) and Zenkert (1995). Here, the theory for an *isotropic* sandwich plate with thick faces is used in order to obtain adequate approximations when the ratio t/d is high. The following non-dimensional expression for the bending and shearing deflection u_{sp} at the central point of a plate is taken from Zenkert (1995), and reads

$$\begin{aligned}
\bar{u}_{\mathrm{sp}} &\equiv \frac{u_{\mathrm{sp}} E L}{P} \\
&= \frac{16}{\pi^2 \bar{w}^2} \sum_{m=1}^{\infty} \sum_{n=1}^{\infty} \frac{1}{mn \bar{K}_m} \left(1 + \frac{\bar{D}_0 \pi^2}{\bar{D}_Q (1 - v_p^2)} \left(\frac{m^2 + n^2}{\bar{b}^2} \right) \right) \\
&\quad \times \sin^2 \left(\frac{m\pi}{2} \right) \sin^2 \left(\frac{n\pi}{2} \right) \sin \left(\frac{m\pi}{2} \frac{\bar{w}}{\bar{b}} \right) \sin \left(\frac{n\pi}{2} \frac{\bar{w}}{\bar{b}} \right),
\end{aligned} \tag{B.1}$$

where the denominator $\bar{K}_m$ is

$$\bar{K}_m = \frac{2\bar{D}_f \bar{D}_0 \pi^6}{\bar{D}_Q (1 - v_p^2)^2} \left(\frac{m^2 + n^2}{\bar{b}^2} \right)^3 + \frac{\bar{D} \pi^4}{(1 - v_p^2)} \left(\frac{m^2 + n^2}{\bar{b}^2} \right)^2 \tag{B.2}$$

and

$$\bar{D}_f \equiv \frac{D_f}{EL^3} = \frac{\bar{t}^3}{12}, \quad \bar{D}_0 \equiv \frac{D_0}{EL^3} = \frac{\bar{t}\bar{d}^2}{2}, \quad \bar{D}_c \equiv \frac{D_c}{EL^3} = \frac{E_{11}^c}{E} \frac{(\bar{d} - \bar{t})^3}{12},$$
$$\bar{D} \equiv 2\bar{D}_f + \bar{D}_0 + \bar{D}_c. \tag{B.3}$$

Here, D_f, D_c, and D are, respectively, the *flexural rigidity* of the facesheet, core and sandwich plate, and an overbar denotes the equivalent non-dimensionalised quantity. For an isotropic core, E_{11}^c is the Young's modulus along the x_1- and x_2-directions.

Upon assuming that the shear modulus of the facesheets much exceeds that of the core, the dimensionless *shearing rigidity* reads

$$\bar{D}_Q \equiv \frac{D_Q}{EL} = \frac{G_{13}^c}{E} \frac{\bar{d}^2}{\bar{d} - \bar{t}}, \tag{B.4}$$
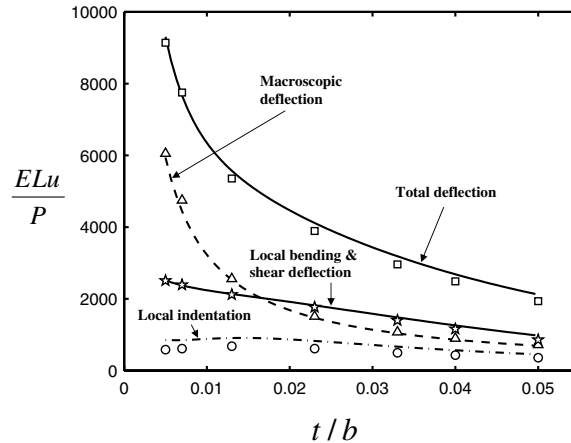
Fig. B.1. Compliances of topology C. The lines give analytical predictions, while the symbols denote the finite element results.

where G_{13}^c is the shear modulus of the core in the 1–3 and 2–3 planes. The Poisson ratio v_p associated with bending of the sandwich plate is taken to equal that of the solid facesheet $v_p = v = 0.3$.

We note from Eqs. (B.1), (B.3), and (B.4) that the plate deflection depends upon the core moduli E_{11}^c and G_{13}^c. The dependence of these moduli upon ρ_c is derived as follows. For topology C, the relative Young's modulus $\overline{E}_{11}^c = \overline{E}_c$ of the foam core scales with the relative density $\overline{\rho}_c$ according to Eq. (7). For topology D, the in-plane relative Young's modulus $\overline{E}_{11}^c$ of the square honeycomb is $\overline{E}_{11}^c = 0.5\overline{\rho}_c$, as given by Eq. (20). The relative out-of-plane shear modulus $\overline{G}_{13}^c$ scales with the relative density according to (Gibson and Ashby, 1997)

$$\overline{G}_{13}^c \equiv \frac{G_{13}^c}{E} = \frac{1}{4(1+v)}\overline{\rho}_c. \tag{B.5}$$

B.2. Local indentation u_{ind}

The local indentation u_{ind} of the loaded outer facesheet in topologies C and D is assumed to be given by the local bending deflection of a loaded facesheet upon an elastic foundation, as for topology B. However, due to the different geometrical configurations, the core layer thickness of topologies C and D is $c = d - t$ (Eq. (42)). The deflection $\overline{u}_{ind}$ is again obtained from Eq. (40). For the choice of a metal foam core (topology C), we assume in Eq. (40) that $\overline{E}_c = \overline{\rho}_c^2$, $v_c = 0.3$, and $\gamma = 2.5$. For topology D, $\overline{E}_c$ is taken to be the normalised out-of-plane Young's modulus of the square honeycomb, $\overline{E}_c \equiv E_{33}^c/E = \overline{\rho}_c$. The two Poisson ratios v_{31}^c and v_{32}^c are taken to be those of the solid itself, $v_{31}^c = v_{32}^c = 0.3$ (Gibson and Ashby, 1997). The Poisson ratio of the square honeycomb is taken as $v_c = 0.3$, and the constant γ is again assumed to have the value $\gamma = 2.5$.

B.3. Accuracy of analytical predictions for topology C: comparison with selected finite element simulations

Finite element calculations of the structural response of topology C under the three-point bend loading defined in Fig. 1 have been performed using the finite element software ABAQUS (version 6.4, 2004). Similar to the FE simulation of topology B in Section 4.1, for the case of topology C the solid facesheets and foam core are modelled using 4-noded shell elements and 8-noded linear brick elements (S4R and C3D8R in the ABAQUS notation). Tie constraints are used to tie the facesheets to the core. Numerical simulations are made for $H/L = 0.175$, $b/L = 0.15$, $d/L = 0.03$, and $w/L = 0.05$. The facesheets and foam core have a Poisson ratio of $v = v_c = 0.3$, whilst the foam core has a Young's modulus of $E_c = 0.01E$. For both the facesheets and core, 14 elements exist along the tube width, 3 elements exist through the core layer thickness, and 123 elements exist along the tube span. As shown in Fig. B.1, excellent agreement is noted between the FE results and the analytical formulae.

Appendix C. Local deflections of topologies *E* and *F*

C.1. Topology E

It is assumed that the local deflection u_l of topology *E* comprises the bending and shearing deflection of the upper sandwich wall u_{sp}, and the local indentation of the loaded outer facesheet u_{ind} upon the sandwich core. (The same assumption was employed for topologies *C* and *D*).

C.1.1. Local bending and shearing deflection u_{sp}

The deflection u_{sp} of the loaded upper sandwich wall is assumed to equal the bending and shearing deflection of a simply supported, *orthotropic* sandwich plate of width *b*. The full solution for the bending and shearing deflection of an orthotropic sandwich plate is outlined by Allen (1969) and Zenkert (1995), and the normalised central deflection of the plate reads

$$\bar{u}_{sp} \equiv \frac{u_{sp}EL}{P} = \frac{16}{\pi^2 \overline{w}^2} \sum_{m=1}^{\infty} \sum_{n=1}^{\infty} \frac{\overline{W}_{mn}}{mn\overline{Z}_{mn}} \sin^2 \left(\frac{m\pi}{2}\right) \sin^2 \left(\frac{n\pi}{2}\right) \sin \left(\frac{m\pi}{2} \frac{\overline{w}}{\overline{b}}\right) \sin \left(\frac{n\pi}{2} \frac{\overline{w}}{\overline{b}}\right), \tag{C.1}$$

where it is assumed that the shear stiffness D_{Q1} of the corrugated core along the prismatic x_1-direction is infinite, as discussed by Allen (1969). The axes with respect to the core are given in Fig. 3b. Expressions for $\overline{W}_{mn}$ and $\overline{Z}_{mn}$ are taken from Zenkert (1995). These quantities depend upon the normalised bending ($\overline{D}_{11}$, $\overline{D}_{22}$), twisting ($\overline{D}_{12}$), and shearing ($\overline{D}_{Q2}$) stiffnesses of the plate cross-section, as given by

$$\overline{D}_{11} = \frac{\bar{t}^3}{6} + \frac{\bar{t}\bar{d}^2}{2} + \frac{\overline{\rho}_c(\bar{d} - \bar{t})^3}{12} \tag{C.2}$$

$$\overline{D}_{22} = \frac{\bar{t}^3 + 3\bar{t}\bar{d}^2}{6\left\{1 - v^2\left(1 - \frac{\bar{t}^3 + 3\bar{t}\bar{d}^2}{6\overline{D}_{11}}\right)\right\}} \tag{C.3}$$

$$\overline{D}_{12} = \frac{\bar{t}^3 + 3\bar{t}\bar{d}^2}{6(1 + v)} \tag{C.4}$$

and

$$\overline{D}_{Q2} \approx 0.521 \frac{S_{sh}\overline{\rho}_c^3}{(1 - v^2)} \frac{\bar{d}^2}{\bar{d} - \bar{t}}. \tag{C.5}$$

The non-dimensional coefficient S_{sh} takes values in the range of 0.4–15, depending upon the facesheet thickness, the shape of corrugation, relative proportions of sandwich cross-section, and the material properties of the component parts. For the present study, the core morphology is chosen as $\omega = 45°$ and $f_c/l_c = 0.5$ with the curvature at the bending corners neglected. The lengthy expression for S_{sh} is omitted and the reader is referred to Libove and Hubka (1951).

The two Poisson ratios associated with the bending of the plate are

$$v_{12} = v \quad \text{and} \quad v_{21} = v\overline{D}_{22}/\overline{D}_{11}. \tag{C.6}$$

C.1.2. Local indentation u_{ind}

For an isotropic sandwich plate, the local indentation of the loaded outer facesheet $\bar{u}_{ind}$ has already been stated by Eq. (40). In the isotropic core, the core is characterised by a Young's modulus E_c, Poisson ratio v_c, and constant factor γ. In the absence of a more accurate formula we make use of Eq. (40) for the orthotropic core and we assume an equivalent Young's modulus E_{eq}^c and Poison ratio v_{eq}^c of

$$E_{eq}^c \equiv E_{33}^c \quad \text{and} \quad v_{eq}^c \equiv (v_{31}^c + v_{32}^c)/2, \tag{C.7}$$

where E_{33}^c is the core Young's modulus in the x_3-direction, and v_{31}^c and v_{32}^c are the Poisson ratios of the core in the 3–1 and 3–2 planes, respectively.

The modulus E_{33}^c of the corrugated core is derived by methods outlined by Cote et al. (2005), giving

$$\overline{E}_{eq}^c \equiv \frac{E_{33}^c}{E} = \frac{1}{6(1-v^2)}\overline{\rho}_c. \tag{C.8}$$

The Poisson ratios v_{31}^c and v_{32}^c are taken to equal v, and the equivalent Poisson ratio reads $v_{eq}^c = v = 0.3$. The parameter γ in Eq. (40) is assumed to equal 2.5 for the corrugated core (recall that this value was accurate for the foam core, see Fig. 7).

C.2. Topology F

It is assumed that the local deflection u_l of the loaded upper wall in topology F equals the bending deflection of a square simply supported *anisotropic* plate of width b. The solution is discussed by Timoshenko and Woinowsky-Krieger (1970), and the non-dimensional local deflection at the central point of the plate is derived as

$$\overline{u}_l \equiv \frac{u_l EL}{P} = \frac{16\overline{b}^4}{\pi^6 \overline{w}^2} \sum_{m=1}^{\infty} \sum_{n=1}^{\infty} \frac{\sin^2\left(\frac{m\pi}{2}\right)\sin^2\left(\frac{n\pi}{2}\right)\sin\left(\frac{m\pi}{2}\frac{\overline{w}}{\overline{b}}\right)\sin\left(\frac{n\pi}{2}\frac{\overline{w}}{\overline{b}}\right)}{mn\{m^4\overline{D}_{22} + 2m^2n^2\overline{H} + n^4\overline{D}_{11}\}}, \tag{C.9}$$

where the sectional properties of the plate are again normalised as $\overline{D}_{22}$, $\overline{D}_{11}$, and $\overline{H}$. The expressions for these quantities with the effect of the transverse contraction included are

$$\overline{D}_{22} = \frac{\overline{t}^3}{12(1-v^2)\left[1 - \overline{\rho}_c + \frac{\overline{t}^3}{(\overline{t}+\overline{d}_c)^3}\overline{\rho}_c\right]}, \tag{C.10}$$

and

$$\overline{D}_{11} = \frac{1}{(1-v^2)}\left[\frac{\overline{t}^3}{12} + \overline{t}\overline{x}^2 + \overline{\rho}_c\frac{\overline{d}_c^3}{12} + \overline{\rho}_c\overline{d}_c\left(\frac{\overline{d}_c + \overline{t}}{2} - \overline{x}\right)^2\right], \tag{C.11}$$

where

$$\overline{x} \equiv \frac{x}{L} = \frac{(\overline{d}_c + \overline{t})\overline{\rho}_c}{2(\overline{t}/\overline{d}_c + \overline{\rho}_c)} \tag{C.12}$$

is the non-dimensional distance from the centre-line of the wall facesheet to the central point of the T section of width d_c, see Fig. 3c. The quantity $\overline{H}$ is

$$\overline{H} = \frac{\overline{t}^3}{12(1-v^2)} + \frac{\overline{\rho}_c\overline{d}_c^3}{24(1+v)}. \tag{C.13}$$

For topology F the overall non-dimensional stiffness is $\overline{S} = 1/(\overline{u}_m + \overline{u}_l)$, where $\overline{u}_m$ and $\overline{u}_l$ are given by Eqs. (14) and (C.9), respectively.

References

ABAQUS Standard User's Mannual, Version 6.4, 2004.

Allen, H.G., 1969. Analysis and Design of Structural Sandwich Panels. Pergamon Press, Oxford.

Ashby, M.F., Evans, A.G., Fleck, N.A., Gibson, L.J., Hutchinson, J.W., Wadley, H.N.G., 2000. Metal Foams: A Design Guide. Butterworth Heinemann, London.

Budiansky, B., 1999. On the minimum weights of compression structures. Int. J. Solids Struct. 36, 3677–3708.

Cote, F., Deshpande, V.S., Fleck, N.A., Evans, A.G., 2005. The compressive and shear responses of the corrugated and diamond core lattice materials. Int. J. Solids Struct, to appear.

Deshpande, V.S., Fleck, N.A., 2001. Collapse of truss core sandwich beam in 3-point bending. Int. J. Solids Struct. 38, 6275–6305.

Evans, A.G., Hutchinson, J.W., Fleck, N.A., Ashby, M.F., Wadley, H.N.G., 2001. The topological design of multifunctional cellular metals. Prog. Mat. Sci. 46, 309–327.

Gibson, L.J., Ashby, M.F., 1997. Cellular Solids: Structure and Properties, Second ed. Cambridge University Press, Cambridge.

Gu, S., Lu, T.J., Evans, A.G., 2001. On the design of two-dimensional cellular metals for combined heat dissipation and structural load capacity. Int. J. Heat Mass Transfer 44, 2163–2175.

Libove, C., Hubka, R.E., 1951. Elastic constants for corrugated-core sandwich plates. NACA TN 2289, Washington.

MathWorks. Matlab user's guide, version 7. 2004.

Meo, F., Merlo, A., de la O Rodriguez, M., Brunner, B., Ippolito, M., 2005. Advanced hybrid mechatronic materials for ultra precise and high performance machining systems design. Proceedings of IPROMS 2005.

Srikantha Phani, A., Mai, S.P., Fleck, N.A., Woodhouse, J., 2006. A prismatic-core design for a milling machine component. Int. J. Mach. Tools Manufact. (submitted for publication).

Thomsen, O.T., 1993. Analysis of local bending effects in sandwich plates with orthotropic face layers subjected to localised loads. Int. J. Composite Struct. 25, 511–520.

Timoshenko, S.P., Gere, J.M., 1972. Mechanics of Materials. D. Van Nostrand, New York.

Timoshenko, S.P., Woinowsky-Krieger, S., 1970. Theory of Plates and Shells. Mc Graw-Hill, Singapore.

Vlasov, V.Z., Leont'ev, N.N., 1960. Beams, Plates and Shells on Elastic Foundations. Moscow (English translated by Israel Program for Scientific Translation, Jerusalem, 1966).

Wadley, H.N.G., Fleck, N.A., Evans, A.G., 2003. Fabrication and structural performance of periodic cellular metal sandwich structures. Int. J. Composites Sci. Tech. 63, 2331–2343.

Wicks, N., Hutchinson, J.W., 2001. Optimal truss plates. Int. J. Solids Struct. 38, 5165–5183.

Zenkert, D., 1995. An Introduction to Sandwich Construction. Engineering Materials Advisory Services Ltd, United Kingdom.

Zok, F.W., Rathbun, H.J., Wei, Z., Evans, A.G., 2003. Design of metallic textile core sandwich panels. Int. J. Solids Struct. 40, 5707–5722.